frontiers in Materials

ORIGINAL RESEARCH
published: 23 December 2021
doi: 10.3389/fmats.2021.743112

Facile Fabrication and Properties of Super-hydrophobic MgAl-LDH Films With Excellent Corrosion Resistance on AZ31 Magnesium Alloy

Xing Han[1], Jia Hu[1,2], Yong-Qin Wang[1], Tian-Bing Xiao[3]*, Wei Xia[3]*, Yan-Ning Chen[1] and Liang Wu[1,2]*

[1]College of Materials Science and Engineering, Chongqing University, Chongqing, China, [2]National Engineering Research Center for Magnesium Alloys, Chongqing University, Chongqing, China, [3]People's Hospital of FengJie, Chongqing, China

OPEN ACCESS

Edited by:
Yong A. Zhang,
University of Science and Technology Beijing, China

Reviewed by:
Sheng Lu,
Jiangsu University of Science and Technology, China
Pavlo Maruschak,
Ternopil Ivan Pului National Technical University, Ukraine
Songqin Xia,
North China Electric Power University, China

***Correspondence:**
Jia Hu
hujia827@cqu.edu.cn
Tian-Bing Xiao
70441840@qq.com
Wei Xia
690065056@qq.com

Specialty section:
This article was submitted to Structural Materials, a section of the journal Frontiers in Materials

Received: *17 July 2021*
Accepted: *22 November 2021*
Published: *23 December 2021*

Citation:
Han X, Hu J, Wang Y-Q, Xiao T-B, Xia W, Chen Y-N and Wu L (2021) Facile Fabrication and Properties of Super-hydrophobic MgAl-LDH Films With Excellent Corrosion Resistance on AZ31 Magnesium Alloy. Front. Mater. 8:743112. doi: 10.3389/fmats.2021.743112

A super-hydrophobic anti-corrosion film was facilely prepared *via in situ* growth of layered double hydroxides (LDHs) on the etched AZ31 magnesium alloy and then modification by 1H, 1H, 2H, 2H-perfluorooctyltrimethoxysilane (PFOTMS) in this work. The morphology, structure, composition, surface roughness and water contact angles (WCA), and the anti-corrosion performance of the samples were investigated. The results revealed that the micro/nano hierarchical surface morphology of the films was composed of island structures obtained after chemical etching and MgAl-LDH nanowalls grown *in situ*. The best hydrophobicity (CA = 163°) was obtained on the MgAl-LDHs with the maximum surface roughness. Additionally, the potentiodynamic polarization, electrochemical impedance spectroscopy, and immersion test indicated that the super-hydrophobic LDH films provided better corrosion resistance to AZ31 magnesium alloy due to the double-protection derived from the LDHs and super-hydrophobic properties. Furthermore, the contact angle could be kept at above 140° after dipped in 3.5 wt% NaCl solution for 6 days.

Keywords: LDH films, super-hydrophobic, corrosion protection, magnesium alloys, properties

1 INTRODUCTION

Magnesium alloys have been applied in automotive, aerospace fields, and military equipment on a large scale because of low density, high thermal conductivity, good electromagnetic shielding, and easy recyclability (Xie et al., 2018; Yao et al., 2020; Yang et al., 2021). However, magnesium alloys are vulnerable to aggressive media due to their high chemical activity (Song et al., 2021), which severely restricts the potential application of magnesium alloys. So, a variety of surface-modification methods to enhance their corrosion resistance have been proposed in recent decades, such as micro-arc oxidation (Xu et al., 2021), friction stir processing, laser surface modification, physical vapor deposition, (Zhang et al., 2020), and so on. However, it has been reported that these above methods not only needed to use expensive equipment, but also the formed coatings showed a porous structure. Moreover, this coatings prepared *via* the above methods only can provide a passive physical barrier function (Bocchetta et al., 2021), which cannot significantly improve the corrosion resistance. Currently, an active anticorrosion layered double hydroxides (LDHs) films, which can store corrosion inhibitor, have attracted extensive attention due to that corrosion inhibitors can spread to the metal surface around the defect and react with the

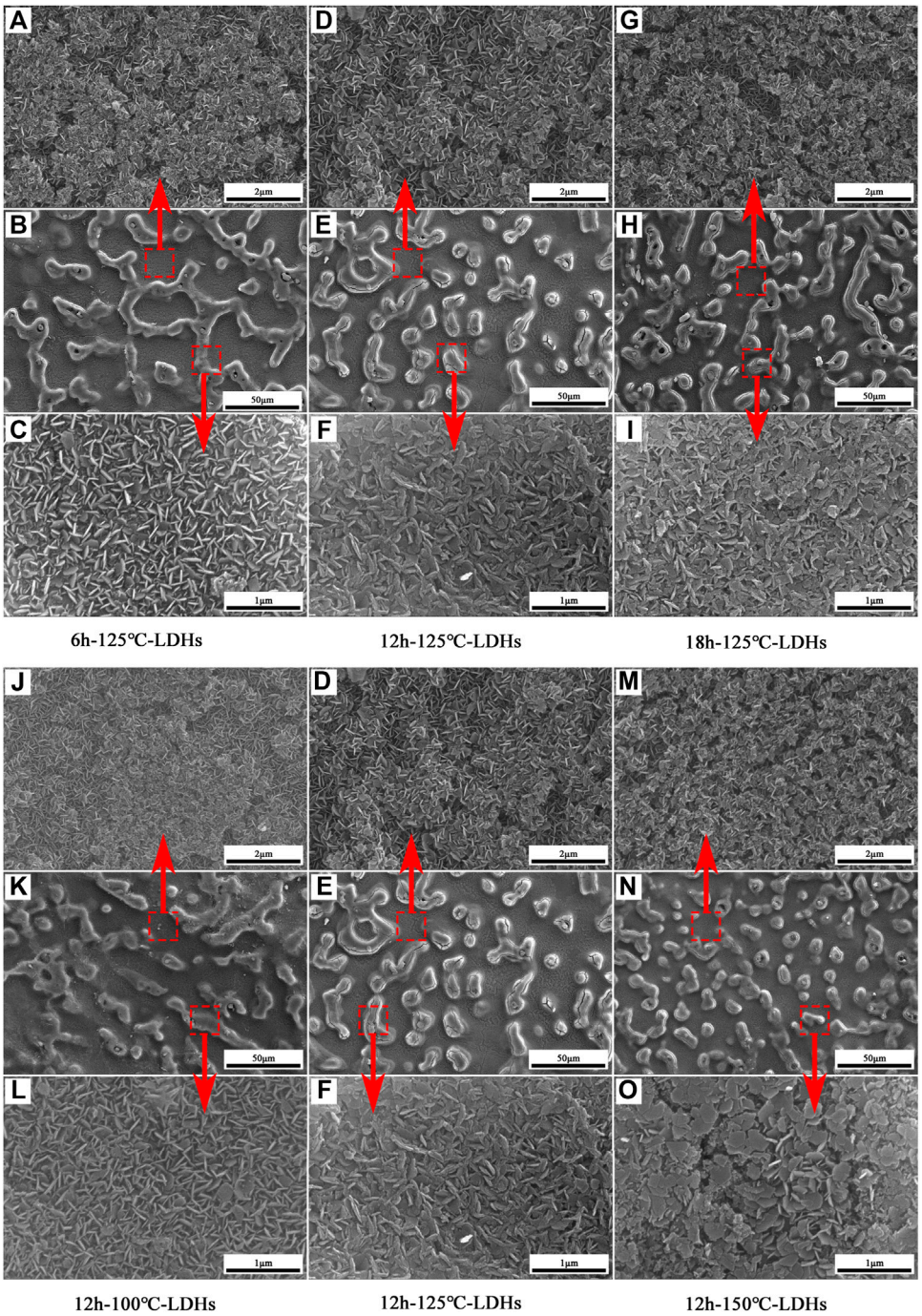

FIGURE 1 | SEM images of different specimens: **(A,B,C)** 6h-125°C-LDHs, **(D,E,F)** 12h-125°C-LDHs, **(G,H,I)** 18h-125°C-LDHs, **(J,K,L)** 12h-100°C-LDHs, and **(M,N,O)**12 h-150°C-LDHs.

substrate to form the stable precipitations on the defect, aiming to heal films in time (Zhang et al., 2018). LDH film loaded with corrosion inhibitors can provide both passive physical barrier function and active corrosion resistance to the magnesium alloy, because the film itself acts as a strong physical barrier and LDHs possess the anion-exchange capacity.

LDHs, known as hydrotalcite-like compounds, is a class of nanocarrier loaded with corrosion inhibitor. The unique hierarchical structure of LDHs endows it with anion-exchange capability (Chen J. et al., 2021; Wu et al., 2021). Hence, an active protective LDH film grown *in situ* on the surface of the metal substrate can present significant advantages. The LDH films require neither the complicated molecular design nor the

sophisticated preparation process. Furthermore, the LDH films can capture aggressive anions and release corrosion inhibitors based on the ion exchange performance (Chen et al., 2020), and the continuous LDH films itself also can provide a firm physical barrier for magnesium alloys, effectively preventing the corrosive medium from invading into the substrate (Cao et al., 2018). However, anionic inhibitors loaded in LDHs will rapidly release when exposing to external high concentration solution environment or immersing corrosion solution for a long time, directly leading to a severe decline in corrosion resistance of the LDH films. Generally speaking, the LDH films grown on metal substrate display non-closed structure. Furthermore, the LDH structure can provide not only the accommodation for corrosion mediums but also the channel for corrosion mediums passing through to the substrate (Chen et al., 2013). Thereby, the corrosion protection of single LDH film for metal substrate is limited. Inspired by outstanding water-repellency and self-cleaning ability of these natural super-hydrophobic surface (Xie et al., 2018), researchers have successfully designed and fabricated artificial super-hydrophobic surface on metallic substrate. The non-wetting performance of super-hydrophobic surface can effectively prevent the attachment of corrosion solution. So, it is anticipated that the design of super-hydrophobic surface on LDHs can impede the attack of corrosive liquid, furthermore improving the corrosion resistance of LDH film. Unfortunately, the researches on the super-hydrophobic LDH films are limited in this field. Moreover, the preparing process of the super-hydrophobic LDH films reported in previous literatures was relatively complex and the stability of super-hydrophobicity was not deeply discussed. Wang and co-workers (Wang et al., 2020) obtained the load-inhibitors MgAl-LDH films on the porous anodized Mg alloys *via in situ* growth method and then post-sealing it by a super-hydrophobic coating, showing active corrosion protection property. Wu et al. (Wu et al., 2019) used different kinds of low surface energy substances to modify LDHs *in situ* grown on anodized AZ31 Mg alloy. The result suggested that LDHs modified by fluoroalkylsilane can offer a better corrosion protection for AZ31 Mg alloy than the fatty acid with long carbon chains. Chen et al. (Chen et al., 2006) reported that the LDH crystallite orientation prepared on a PAO/Al substrate can be tailored by controlling the hydrothermal crystallization temperature and time, further providing the appropriate micro and nanostructures to obtain the super-hydrophobic LDH films. Similarly, the orientation of the LDH microsheet layer produced on Al-enriched Mg alloys was tailored by adjusting the hydrothermal temperature, time, and pH to produce a water-repellent surface after modification with fluorinated silane (Zhang et al., 2015). Therefore, in our work, a facile method was used to fabricate directly super-hydrophobic anti-corrosion LDH films on AZ31 Mg alloy. To be specific, LDH nanosheets was formed on etched AZ31 surface by *in situ* hydrothermal crystallization method, which provided a micro/nanostructure for the preparation of super-hydrophobic surface. Then, the LDH films were modified by 1H, 1H, 2H, 2H-perfluorooctyltrimethoxysilane (PFOTMS) to lower the surface energy. The influences of the hydrothermal treatment time and temperature on the surface morphology and corrosion resistance of the super-hydrophobic LDH films were investigated, and the stability of super-hydrophobicity was analyzed. The results demonstrated that the super-hydrophobic LDH films improved significantly the corrosion resistance of Mg alloy and displayed excellent stability of super-hydrophobicity in corrosive liquid.

2 EXPERIMENTAL SECTION

2.1 Materials

Commercial cast magnesium alloy AZ31 ingot was cut into 16 mm × 16 mm × 5 mm cubes by wire-cutting. $Al(NO_3)_3{\cdot}9H_2O$, $NaNO_3$, NaOH, and ethanol were purchased from Chongqing Huanghui Chemical Dangerous Goods Sales Co., Ltd, and 1H, 1H, 2H, 2H-perfluorooctyltrimethoxysilane was ordered from Aladdin Industrial Corporation. All reagents were used as received without further purification. All solutions were prepared with deionized water.

2.2 Pretreatment of AZ31 Mg Alloy Cubes

The AZ31 specimens were sequentially polished with emery sand paper of grades 400, 800, and 1,200 to obtain bright mirror plane, ultrasonically cleaned in absolute ethyl alcohol for 10 min, and then dried in warm stream. The dried substrates were etched in 6.5 wt. % HNO_3 for 20 s at room temperature, aiming to mainly remove oxide and build the micro-nano rough structure on AZ31 Mg alloy surface.

2.3 Preparation of MgAl-LDHs

The MgAl-LDH films were prepared by *in situ* hydrothermal crystallization treatment on chemical etched AZ31 magnesium alloy substrate. $Al(NO_3)_3{\cdot}9H_2O$ (0.01 mol) and $NaNO_3$ (0.005 mol) were sequentially dissolved in deionized water with continuous magnetic stirring to form a clear solution with a total volume of 100 ml. Then, the pH of the solution was adjusted to 10.7 by adding 4.0 M NaOH solution dropwise further to get turbid liquids. The etched specimens were vertically placed in Teflon-lined stainless steel autoclaves containing mixture solution, and then the hydrothermal treatment was carried out at 125°C for different times (6, 12, 18 h) or at different temperatures (100°C, 125°C, 150°C) for 12 h. Finally, the as-prepared specimens were removed with tweezers, rinsed with running deionized water and ethanol, and dried with a warm air flow. The obtained samples were denoted as 6h-125°C-LDHs, 12h-125°C-LDHs, and 18h-125°C-LDHs at the same temperature 125°C, 12h-100°C-LDHs, 12h-125°C-LDHs, and 12h-150°C-LDHs at the same time 12 h, respectively.

2.4 Fabrication of the Super-hydrophobic Surface

The super-hydrophobicity of MgAl-LDH film surface was obtained by immersing in the mixed solution containing 2 ml PFOTMS and 100 ml ethanol at 60°C for 1 h in the oven. After

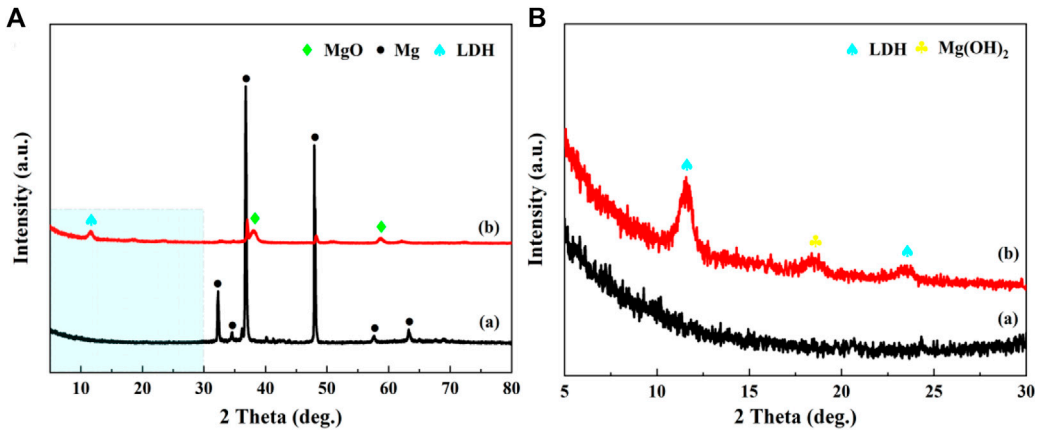

FIGURE 2 | (A) Wide-angle XRD pattern of AZ31 sample (curve a: Mg substrate) and small-angle XRD pattern of MgAl-LDHs (curve b: MgAl-LDHs); **(B)** the magnification of Figure 2A from 5° to 30°.

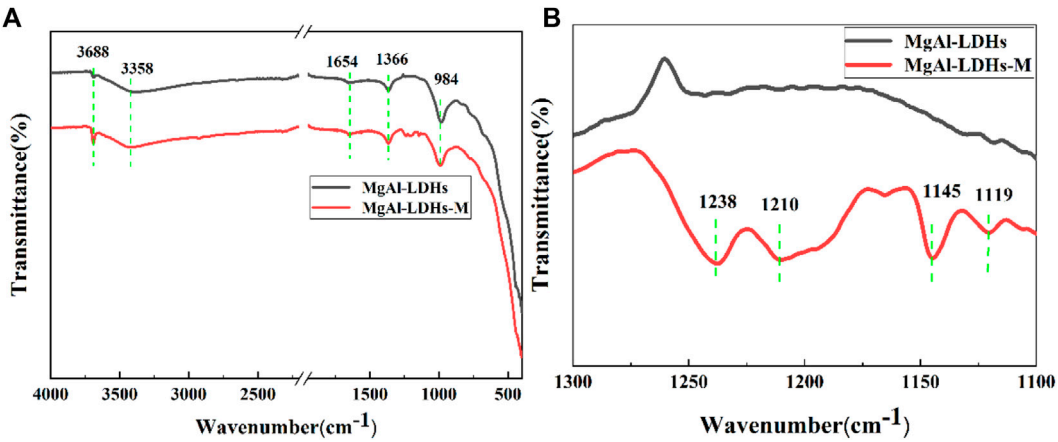

FIGURE 3 | (A,B) FT-IR spectra of different samples; please note that Figure 3B is the magnification of Figure 3A from 1300 cm^{-1} to 1100 cm^{-1}.

immersion, the as-prepared samples were continually dried at 60°C for 1 h in the oven. The final products were labelled as 6h-125°C-LDH-M, 12h-125°C-LDH-M, 18h-125°C-LDH-M, 12h-100°C-LDH-M, and 12h-150°C-LDH-M, respectively.

2.5 Surface Characterization

The surface morphology of different samples was obtained by scanning electronic microscopy with an EDX attachment (SEM, Thermo Scientific Quattro S) under electron accelerating voltage of 20 kV. The SEM specimens were sputtered with gold to avoid discharge problems before performing the SEM observation. A three dimensional laser scanning confocal microscope system (OLS40-SU, Olympus, Japan) was used for surface roughness measurements of different samples. The crystal structure of the samples was characterized by the X-ray diffraction (XRD, Rigaku D/Max 2,500X) with Cu Kα radiation (λ = 1.5406 Å) at 40 kV and 30 mA, within the range of 2θ = 5–80°. The wide-angle XRD and small-angle XRD spectra was performed at a scanning rate of 10°/min and 1°/min, respectively. Fourier transform infrared spectroscopy (FTIR, Nicolet IS5 Thermo Scientific, United States) spectra were obtained in the range of 4,000–400 cm^{-1} at a resolution of 4 cm^{-1} using 16 scans. Static water contact angles (CA) were measured by a sessile drop with 10 μl liquid droplet using a contact angle meter (SDC-100, SINDIN, China) at an ambient temperature. The CA values reported in the form of mean values were calculated from measurements made on at least three different locations of each sample.

2.6 Electrochemical Test

To evaluate corrosion resistance of different specimens, polarization curves and electrochemical impedance spectra (EIS) were performed successively on electrochemical workstation (PARSTAT4000A, Princeton, America) with a three-electrode corrosion cell at room temperature. The cell was placed in a Faraday cage to avoid external electromagnetic

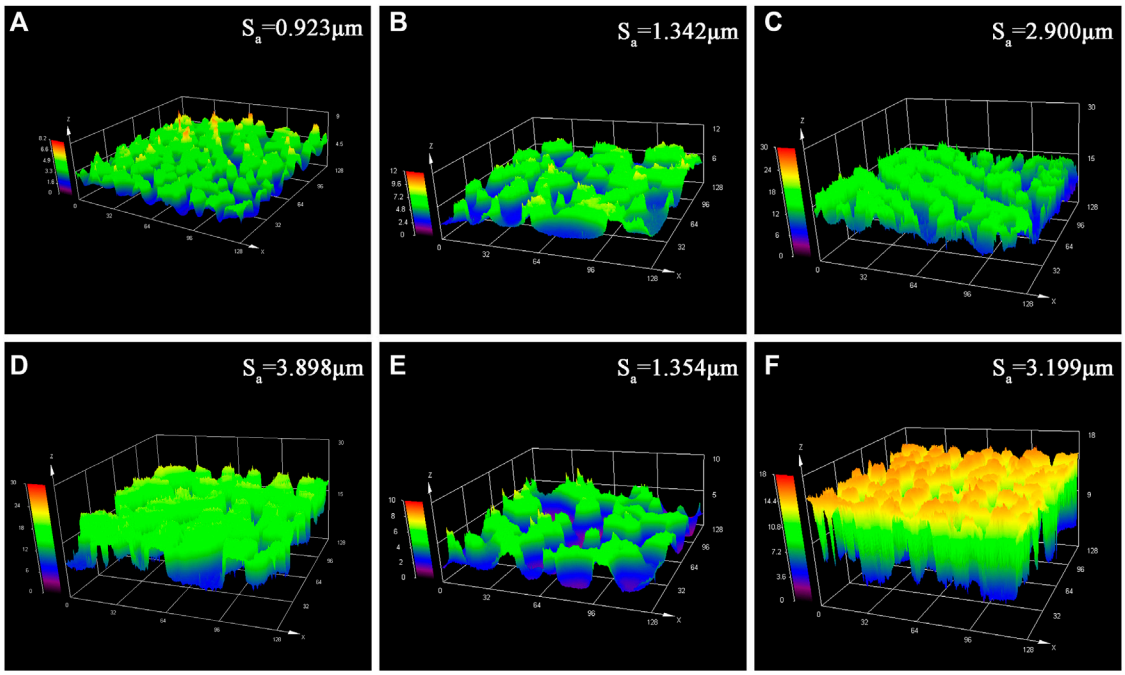

FIGURE 4 | Laser microscopy images of different samples: **(A)** etched Mg-substrate, **(B)** 6 h-125°C-LDHs, **(C)** 18 h-125°C-LDHs, **(D)** 12 h-125°C-LDHs, **(E)** 12 h-100°C-LDHs, and **(F)** 12 h-150°C-LDHs.

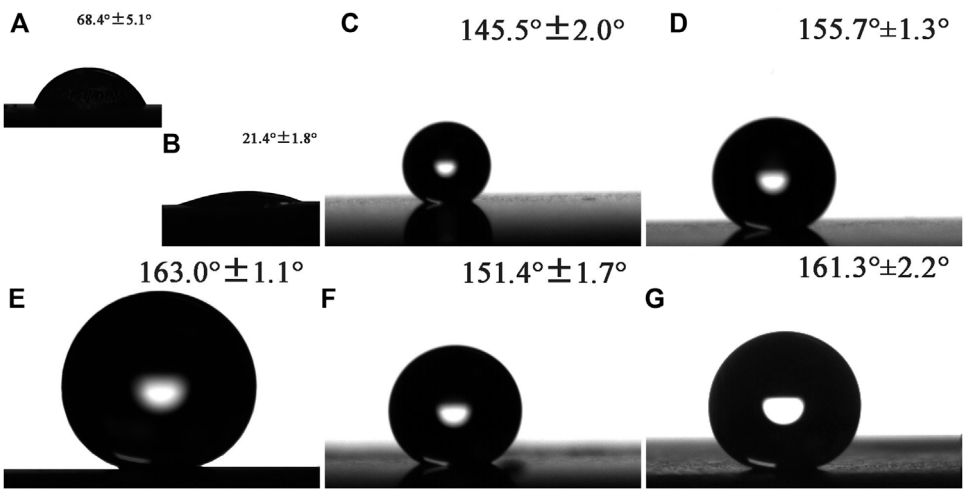

FIGURE 5 | Shapes of water droplets on the surface of different samples and the corresponding water CA: **(A)** etched Mg substrate, **(B)** MgAl-LDHs, **(C)** 6 h-125°C-LDHs-M, **(D)** 18 h-125°C-LDHs-M, **(E)** 12 h-125°C-LDHs-M, **(F)** 12 h-100°C-LDHs-M, and **(G)** 12 h-150°C-LDHs-M.

interference in the environment. The working electrode was as-prepared sample with exposure area of 1 cm^2, and the Ag/AgCl sat. KCl electrode with a Luggin capillary and platinum sheet were used as the reference electrode and the counter electrode, respectively. The samples were immersed in 3.5 wt% NaCl solution for 30 min to reach a steady state before they were tested. Open circuit potential was measured firstly, and then EIS measurement was performed in the frequency range from 100 kHz to 10 mHz using a sine signal with an amplitude of 10 mV. EIS data were fitted by using different equivalent circuits with ZSimpWin software, and the quality of the EIS fitting results was evaluated by the value of χ^2 (Chen L.-Y. et al., 2021). The polarization curves were measured from −0.5 to +0.5 versus OCP at a scanning rate 1 mV/s. Each of the electrochemical test was repeated at least three times to guarantee the reproducibility.

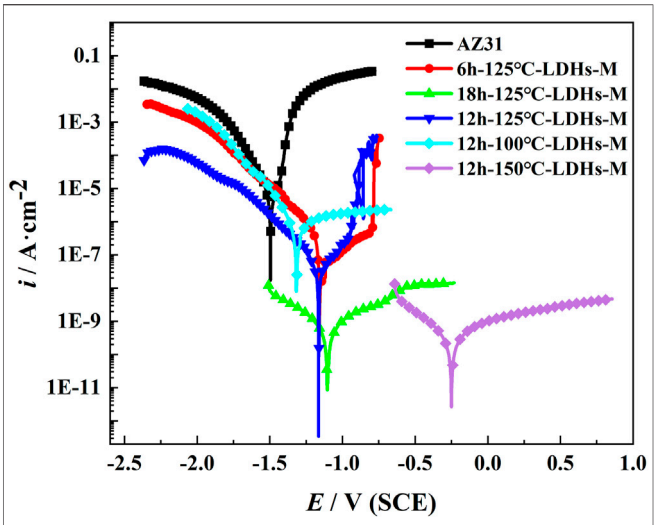

FIGURE 6 | Polarization curves of different samples in 3.5 wt% NaCl solution.

2.7 The Stability of Super-hydrophobicity

The chemical stability of the prepared super-hydrophobic LDH films was studied by immersing the samples in 3.5 wt% NaCl solution for 6 days, and the static CA of water was measured every day. Besides, the surface morphology of samples was observed by SEM during the immersing process.

3 RESULTS AND DISCUSSION

3.1 Surface Characterization

Figure 1 depicts the SEM images of different samples. It can be seen clearly from **Figure 1** that different specimens possessed hump island structures under a low resolution because of the etched AZ31 Mg alloy. The hexagonal plate-like LDH nanosheets grown on the surface of AZ31 Mg alloy were observed in SEM images of the high resolution. The platelets of LDH crystallites were perpendicular to the substrate and covered the entire metal surface. As can be seen from the high-resolution SEM diagrams, morphology on the islands showed significantly different structures as the hydrothermal time extended. According to **Figure 1C**, the island structure of 6 h–125°C-LDHs sample was composed of laminate interlocked LDH nanoplates vertical to substrate. As the growth time increased, the dense and flat LDH nanosheets on the island were shown in **Figure 1F, I**. According to **Figure 1L, F, O**, the similar changes in the morphology of the LDH nanoplates can be found as the hydrothermal temperature ascended. From **Figure 1**, the morphology of 12 h–150°C-LDH film obviously consisted of flat-lying hexagonal LDH nanosheets. The SEM images revealed that the micro/nanoscale coarse structure of metal surface was composed of the small island obtained after chemical etching and the LDH nanosheets *in situ* grown. A cross-sectional view of the MgAl-LDH films (**Supplementary Figure S1A**) clearly demonstrated that a layer of the LDH crystals with a thickness of about 20.2 μm was assembled on the etched magnesium alloy substrate. This observation could be confirmed by energy dispersive X-ray (EDX) analysis, presented in **Supplementary Figure S1B**. Along EDX line scans over the LDH layer and a part of the metal substrate, the Mg Kα profile of the EDX increased with the depths. However, the O Kα profile of the EDX rapidly decreased to almost zero at the interface of the LDH films and the metal matrix, indicating the absence of O species inside the substrate.

TABLE 1 | Electrochemical parameters estimated from the polarization data in **Figure 6**.

Samples	E_{corr}/V (SCE)	i_{corr}/μA cm^{-2}
AZ31	−1.494	6.19
6 h-125°C-LDHs-M	−1.129	6.39×10^{-2}
18 h-125°C-LDHs-M	−1.105	8.55×10^{-4}
12 h-125°C-LDHs-M	−1.062	6.20×10^{-3}
12 h-100°C-LDHs-M	−1.311	7.85×10^{-1}
12 h-150°C-LDHs-M	−0.241	2.74×10^{-4}

3.2 Structure and Composition of LDH Films

The XRD patterns of treated hydrothermally sample and AZ31 Mg alloy substrate sample were shown in **Figure 2A, B**, respectively. As can be seen from **Figure 2A**, the peaks around 32°, 37°, and 48° were contributed to the reflection peaks from AZ31 Mg alloy substrate. In addition, the peaks around 38° and 58° of samples belonged to the reflection peaks of MgO. The peaks belonged to LDH films cannot be clearly observed in that the intensity of the peaks from AZ31 substrate was extremely high. Therefore, the more delicate pattern of **Figure 2A** from 5° to 30° was shown in **Figure 2B**. According to **Figure 2B**, new peaks from the treated hydrothermal samples were found, suggesting the change of the crystal structure on metal surface. As can be seen from **Figure 2B**, the characteristic peak at around 18° was assigned to the reflection peak of $Mg(OH)_2$. In addition, the peaks at about 11.6° and 23.5° corresponded to the (003) and (006) planes of MgAl-LDHs, indicating a typical layered structure of LDHs (Tang et al., 2019). The d-spacing of 0.863 nm corresponding to the (003) plane of LDH film was obtained based on the Bragg's law ($2d \cdot \sin\theta = n \cdot \lambda$). The height of the interlayered corridor was almost consistent with the reported literatures (Cao et al., 2018). Through the above analysis, it was concluded that the MgAl-LDHs was successfully prepared on the surface of the AZ31 substrate.

Figure 3A presents the FT-IR spectra of MgAl-LDHs and MgAl-LDHs-M (MgAl-LDHs modified by PFOTMS) on AZ31 metal surface within the 400–4,000 cm^{-1} region, respectively. It can be seen from **Figure 3A** that the sharp absorption peak at approximately 3,688 cm^{-1} and the broad peak at about 3,358 cm^{-1} were ascribed to water molecules absorbed physically in LDHs and metal hydroxyl groups on the LDHs surface, respectively (Zhang et al., 2018). The peak at around 1,654 cm^{-1} can be attributed to the bending vibration of crystal water between the LDH layers. In addition, the band

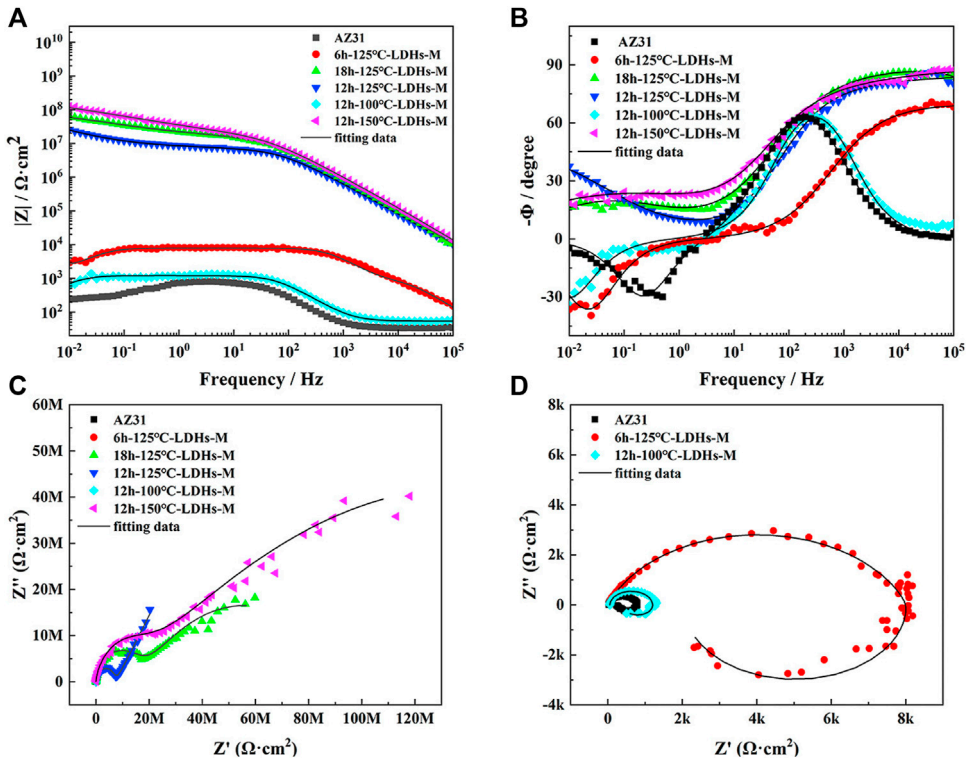

FIGURE 7 | (A) Impedance-frequency Bode plots, **(B)** phase-frequency Bode plots, **(C)** Nyquist plots of different samples in 3.5 wt% NaCl solution after immersion for 30 min, and **(D)** the magnifying graph of **(C)**.

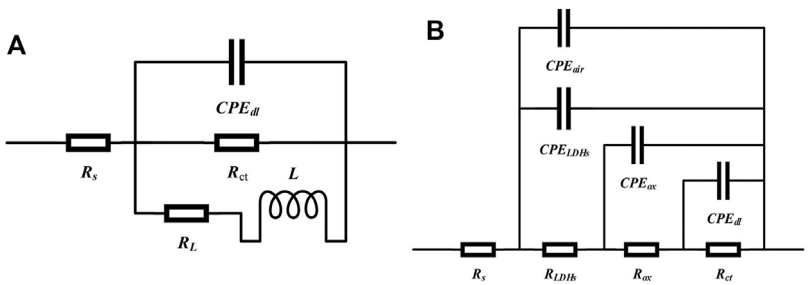

FIGURE 8 | The equivalent circuits used to simulate EIS data of **(A)** AZ31 substrate, 6h-125°C-LDHs-M, and 12h-100°C-LDHs-M; **(B)** 12 h-125°C-LDHs-M, 18 h-125°C-LDHs-M, and 12 h-150°C-LDHs-M after immersion in 3.5 wt% NaCl solution for 30 min.

observed at 1,366 cm^{-1} can be assigned to the stretching vibration of the interlayer NO_3^- in MgAl-LDHs. The intensity of the peaks observed in the range 1,100–1300 cm^{-1} was weak, thus enlarging this range to obtain more refined data in **Figure 3B**. The emerging new absorption peaks that belonged to MgAl-LDHs-M were observed in **Figure 3B**. It was reported in the previous literatures that the absorption bands in 1,100–1,300 cm^{-1} corresponded to the presence of C-F groups (Zhang et al., 2015), and the emerging absorption peaks at around 1,273, 1,191, 1,134, and 1111cm^{-1} were assigned to the vibration of C-F_2 groups (Pazokifard et al., 2012). Thus, **Figure 3B** presents that the two bimodal absorption bands that belonged to MgAl-LDHs-M (1,238, 1,210 cm^{-1} and 1,145, 1119 cm^{-1}) were attributed to the stretching vibration of C-F_2 groups. The above results demonstrated that LDH films were prepared successfully on metal surface, which were in good agreement with the XRD results. It also could be concluded that LDH films were modified successfully by PFOTMS.

TABLE 2 | Fitted parameters of the EIS spectra of the bare AZ31 and coated samples using the same equivalent circuits shown in **Figure 8A**.

Parameters	AZ31	6h-125°C-LDHs-M	12h-100°C-LDHs-M
R_s (Ω·cm^2)	3.33E+01	3.53E+01	2.96E+01
R_{ct} (Ω·cm^2)	7.47E+02	8.91E+03	1.27E+03
CPE_{dl} Y_{dl} (F·cm^{-2})	8.19E-06	2.84E-07	3.24E-06
n_{dl}	9.44E-01	8.61E-01	9.26E-01
R_L (Ω·cm^2)	3.32E+02	2.82E+03	4.17E+02
L (H·cm^2)	4.44E+02	4.14E+04	1.33E+04
χ^2	3.03E-03	3.32E-03	3.51E-03

3.3 Roughness and Wetting Properties of Films

Supplementary Figure S2 showed clearly that different specimens possessed almost the same surface morphologies at the very low resolution, which were composed of a great number of small hump islands. The small island structures offered micro-scale roughness to the super-hydrophobic films. Similarly, LDH nanosheets grown *in situ* on the etched Mg substrate played an important role on the effect of surface roughness. So the 3D roughness profiles of different samples obtained by a laser microscope were shown in **Figure 4**. The etched AZ31 substrate showed a surface roughness of 0.923 μm. As can be seen clearly from **Figure 4**, the surface roughness of these samples treated hydrothermally showed a remarkable increase. The surface roughness of 6h-125°C-LDHs, 12h-125°C-LDHs, and 18h-125°C-LDHs corresponded to Sa = 1.342μm, Sa = 3.898 μm, and Sa = 2.900 μm, respectively. It can be found that the roughness rises first and then decreases with the extension of hydrothermal treatment time. Meanwhile, the surface roughness has a similar change with increasing temperature. The surface roughness of samples treated hydrothermally was significantly increased compared to the etched magnesium alloy, which was attributed to the combination of microscale coarse structure resulting from the etching and nanoscale coarse structure resulting from hydrothermal treatment.

The surface wettability of different samples was evaluated by the CA measurements, and the corresponding CA results were shown in **Figure 5**. The CA of etched metal substrate was 68.4° ± 5.1°, indicating the hydrophilic nature. The water CA of MgAl-LDH film decreased remarkably to 21.4° ± 1.8° compared with the etched substrate, which can be attributed to the increased roughness of the surface because of the existence of LDH nanosheets. After the LDH films were modified by PFOTMS, the LDHs sample almost presented super-hydrophobicity with a CA of more than 150°. It was worth noting that the water CA of 12h–125°C-LDHs-M was the largest, upping to 163.0° ± 1.1°, and the corresponding roughness was also the maximum. The roughness results in **Figure 4** strongly supported the wettability results, revealing that the CA value increased with the roughness under certain conditions. The combination of the roughness in **Figure 4** with the CA in **Figure 5** was in perfect agreement with this conclusion. The corresponding theoretical foundation was presented as follows. Wenzel investigated the relationship between surface roughness and water CA and proposed the theoretical Wenzel equation.

$$\boldsymbol{cos\theta w = r \cdot cos\theta o} \quad (1)$$

where θ_w means the Wenzel CA, θ_o represents the water CA on the ideal surface, and r is the so-called surface roughness (the ratio of the actual surface area to the projected surface area). Based on the above equation, it can be concluded that θ_o will decrease with increasing the surface roughness, when $\theta_w < 90°$; θ_o will increase with increasing the surface roughness, when $\theta_w > 90°$. So, the results of **Figure 5** were in good agreement with the results of **Figure 4**.

3.4 Anti-corrosive Performance

3.4.1. Polarization Characterization

Figure 6 shows the polarization curves of AZ31 substrate and LDH films modified by PFOTMS immersed in 3.5 wt% NaCl aqueous solution for 30 min. According to **Figure 6**, AZ31 exhibited the most negative corrosion potential with the highest corrosion current density among all samples. MgAl-LDHs-M samples presented more positive E_{corr} and lower I_{corr}, which were attributed to the blocking of corrosion media by LDH nanosheets and super-hydrophobic surfaces. Generally speaking, the corrosion potential is a thermodynamic parameter, and the more positive the corrosion potential represents better corrosion protection

TABLE 3 | Fitted parameters of the EIS spectra of coated samples using equivalent circuits shown in **Figure 8B**.

Parameters		12 h-125°C-LDHs-M	18 h-125°C-LDHs-M	12 h-150°C-LDHs-M
R_s (Ω·cm^2)		**3.89E+01**	**5.81E+01**	**4.50E+01**
CPE_{air}	Y_{air} (F·cm^{-2})	1.46E-10	1.58E-10	1.09E-10
	n_{air}	9.75E-01	1.00E+00	1.00E+00
R_{LDHs} (Ω·cm^2)		1.21E+04	1.89E+07	1.74E+07
CPE_{LDHs}	Y_{LDHs} (F·cm^{-2})	4.29E-10	2.20E-09	8.14E-10
	n_{LDHs}	9.22E-01	5.12E-01	8.00E-01
R_{ox} (Ω·cm^2)		8.94E+06	6.85E+07	2.69E+08
CPE_{ox}	Y_{ox} (F·cm^{-2})	6.65E-09	5.23E-08	6.68E-08
	n_{ox}	3.14E-01	4.91E-01	4.72E-01
R_{ct} (Ω·cm^2)		—	—	—
CPE_{dl}	Y_{dl} (F·cm^{-2})	—	—	—
	n_{dl}	—	—	—
χ^2		1.28E-03	3.03E-03	2.49E-03

"/" represents that low-frequency data were not well-fitted because the parameter is out of the frequency range.

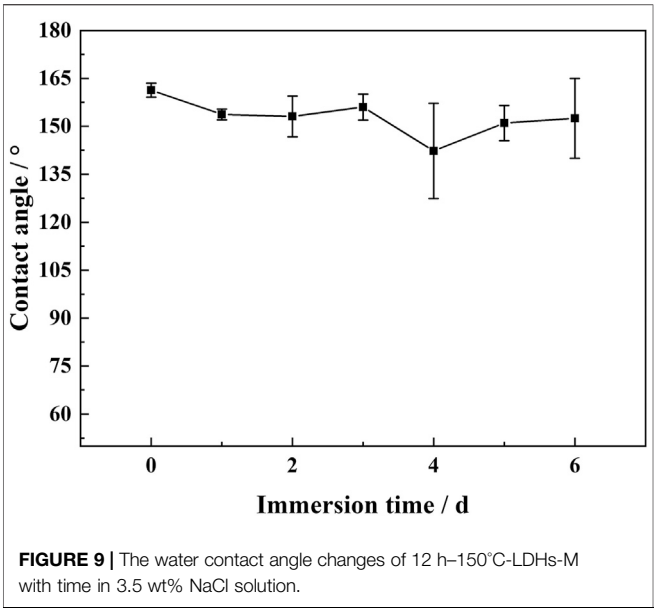

FIGURE 9 | The water contact angle changes of 12 h–150°C-LDHs-M with time in 3.5 wt% NaCl solution.

effect; the corrosion current density is the kinetic parameter, and lower corrosion current densities correspond to lower corrosion rates. The strong polarization area of the polarization curve was selected for obtaining the corrosion potential and the corrosion current density by the Tafel extrapolation method. The values of E_{corr} and I_{corr} of each sample obtained by the fitting procedure were shown in **Table 1**.

From **Table 1**, E_{corr} of super-hydrophobic LDH films were apparently higher than that of AZ31 Mg alloy, indicating that MgAl-LDHs-M can block the attack of corrosive liquids. Particularly, the E_{corr} of 12h–150°C-LDHs-M was nearly one order of magnitude than that of AZ31 substrate, upping to −0.241 V. As can be also seen clearly from **Table 1**, the corrosion current density gradually decreased with the LDHs growth time extending. The corrosion current density of 18h–125°C-LDHs-M in the series of different hydrothermal times was nearly four orders of magnitude lower than that of AZ31 Mg alloy, indicating excellent corrosion protection, because the LDH nanosheets grew more dense and compact on the surface of the magnesium alloy. Similarly, the I_{corr} declined with the LDHs growth temperature improving. It was noteworthy that the I_{corr} of 12h–150°C-LDHs-M in the series of different hydrothermal temperatures was the lowest (I_{corr} = 2.74×10^{-4} μA cm^{-2}), implying the extremely good corrosion protection effect. On the basis of the polarization measurements, the corrosion resistance of the AZ31 substrate was effectively enhanced by double protection from super-hydrophobic LDH films.

3.4.2. Electrochemical Impedance Spectra Characterization

According to **Figure 7C, D**, it can be seen that the Nyquist plots of different samples had apparent difference. Usually, the greater arc radius at the high frequency in the Nyquist plots corresponds to better corrosion protection effect. As shown in the Nyquist plots, the super-hydrophobic LDH films had a better corrosion protection compared with AZ31 substrate. To interpret the obtained EIS results clearly, two kinds of equivalent circuits were shown in **Figure 8**. The equivalent circuit in **Figure 8A** was used to simulate the EIS data of AZ31, 6 h-125°C-LDHs-M, and 12 h-100°C-LDHs-M. In this equivalent circuit, R_s represented the resistance of the solution between the reference electrode and the film surface; the parallel of the constant phase element (CPE_{dl}) and the charge transfer resistance (R_{ct}) was used to describe the electrochemical process of the corrosion process; inductance elements (L) and inductive impedance (R_L) were often used to explain the inductive loop that appeared at low frequency, which originated from adsorbed/desorbed intermediates on the electrode surface (Zhou et al., 2015). In the case of the 12 h-125°C-LDHs-M, 18h-125°C-LDHs-M, and 12 h-150°C-LDHs-M system, their EIS data could be fitted by an equivalent circuit with three time constants. The first time constant at higher frequency was attributed to the effect of super-hydrophobic LDH films, represented by a CEP_{LDHs} in parallel with the resistance of LDH films (R_{LDHs}). Considering that the super-hydrophobic film produced a layer of air film, the CPE_{air} was introduced to characterize the trapped air. The second time constant appearing at intermediate frequency may be related to the oxide film produced on the surface of the substrate, expressed by a CEP_{ox} in parallel with the oxide resistance (R_{ox}). The third time constant occurring at low frequency was associated with the electrochemical corrosion process, denoted as CPE_{dl} and R_{ct}.

Based on the above equivalent circuits shown in **Figure 8A**, the data fitting results are listed in **Table 2**. Usually, the error value of χ^2 represents the quality of fitting results, and the value of $\chi 2$ around 10^{-3} or less indicates good fit (Wang et al., 2020; Qin et al., 2021). As can be shown in **Table 2**, the R_{ct} value of 12h–100°C-LDHs-M was slightly higher than that of AZ31 substrate, indicating the limited protection by super-hydrophobic LDH films prepared at 100°C for the Mg substrate. Notably, the 6h-125°C-LDHs-M sample had the maximum R_{ct} value in the three samples that used the equivalent electron circuit shown in **Figure 8A**, approximately 10 times higher than the AZ31, suggesting that the super-hydrophobic LDH films provided effective protection for the magnesium alloy matrix. The results were consistent with that obtained from Nyquist plots in **Figure 7D**. The low frequency inductance loop shown in **Figure 7D** was associated with the dissolution of the substrate.

Based on a more complex circuit model (**Figure 8B**), the fitted EIS data were shown in **Table 3**. Combining the Nyquist diagram and the fitted data, it was found that the super-hydrophobic LDH film provided corrosion protection to metal substrate that can be effectively improved with the extension of hydrothermal treatment time or the increasing of hydrothermal temperature. As for three samples in **Table 3**, n_{air} was almost one and Y_{air} was extremely small, indicating that the air trapped in the film behaved as the dielectric of the pure parallel plate capacitor, which well suppressed the transfer of the charge between the

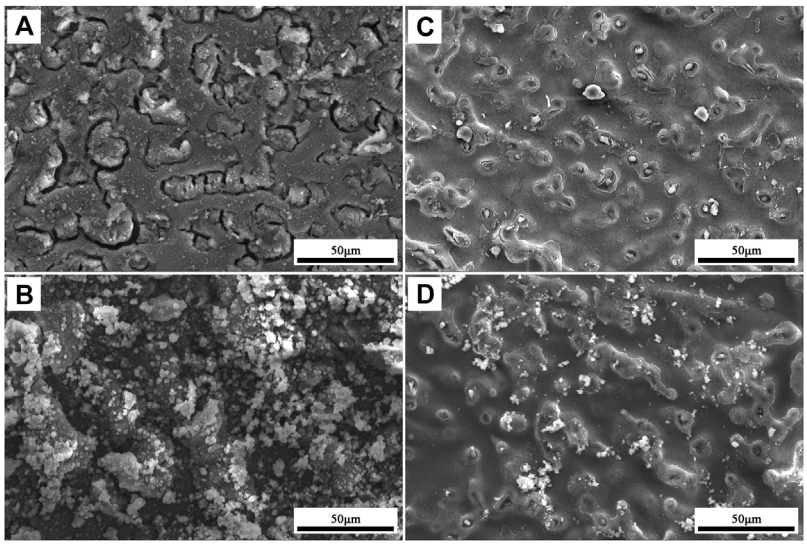

FIGURE 10 | Corrosion morphology of **(A)** AZ31 substrate for immersion 1 h, **(B)** AZ31 substrate for immersion 1 day, **(C)** 12 h-150°C-LDHs-M for immersion 2 days, and **(D)** 12 h-150°C-LDHs-M for immersion 6 days.

electrolyte and the substrate (Wang et al., 2011). Furthermore, the R_{ox} values of all three samples were more than $10^6\ \Omega\ cm^2$, implying that this oxide film provided extremely good protection for the substrate. The oxide film layer between LDHs and the matrix was the last physical barrier preventing corrosive media from invading into the matrix. When the samples do not suffer from corrosion activity, the resistance of the oxide film layer is considered as an important criterion for evaluating the protective performance of the film. It was worth noting that R_{ox} of 12h–150°C-LDHs-M was higher than that of other samples that used the same equivalent circuit shown in **Figure 8B**, which suggested that the oxide layer was much more compact and was protected greatly by the LDH layer and the air film outside. The LDH films played an important role in the whole film, which not only played a physical protection role against the substrate, but also made ion-exchange reactions with the corrosive mediums. The R_{LDHs} values of 18h–125°C-LDHs-M in the series of different hydrothermal times and 12h-150°C-LDHs-M in the series of different hydrothermal temperatures all were approximately three orders of magnitude higher than that of 12h–125°C-LDHs-M, showing the more compact and less porous structure of the LDH films. There was an agreement with results of SEM.

Notably, there were no signs of wetting on the surface of samples shown in **Table 3** after the electrochemical test. It was inferred that only the very slight corrosion has occurred on the surface during the electrochemical test because the surface of the super-hydrophobic samples could not be completely wet during the electrochemical test. Therefore, we cannot obtain accurate the fitting results of R_{ct} and CPE_{dl} since the corrosion process did not completely occurred at this time (Cao et al., 2018). Furthermore, it was also concluded that the corrosion resistance of the three samples shown in **Table 3** was higher than that of the samples presented in **Table 2** from the Nyquist plots and Bode plots shown in **Figure 7**. The above comprehensive analysis demonstrated that the 18h-125°C-LDHs-M in the series of different hydrothermal times and 12h-150°C-LDHs-M in the series of different hydrothermal temperatures had a better corrosion resistance performance than the other samples.

3.5 The Stability of Super-hydrophobicity in Corrosive Liquid

The above results of electrochemical test demonstrated that super-hydrophobic LDH films provided good corrosion protection for AZ31 substrate. Particularly, the 12h-150°C-LDHs-M presented excellent corrosion resistance properties. However, the electrochemical results obtained in a short time can only evaluate corrosion resistance of films in the short term. Therefore, the stability of super-hydrophobic surface was investigated for the evaluation of the long-term corrosion protection of super-hydrophobic films. The 12h-150°C-LDHs-M sample was immersed in the 3.5 wt% NaCl aqueous solution, and the water contact angle and the corrosion morphology were analyzed at 0–6 days to assess the stability of the super-hydrophobicity.

Figure 9 displays the CA changes of 12h–150°C-LDHs-M in 3.5 wt% NaCl solution. It can be apparently observed that the CA of 12h–150°C-LDHs-M still maintained super-hydrophobic property (CA > 150°) within the initial immersion time of 24 h, indicating that the non-wettability of the films remained. Overall, the contact angle of the films can maintain above 140 within 6°days of immersing. From **Figure 10A, B**, it can be inferred that AZ31 immersed in the

3.5°wt % NaCl aqueous solution occurred corrosion after immersion for 1°h; corrosion products precipitated on the surface of AZ31 after immersion for 1°day. As shown in **Figure 10C**, after the 12°h-150°C-LDHs-M immersed in 3.5 wt% NaCl aqueous solution for 48°h, the local area of the film surface began to appear in the corrosion products, and the corresponding water contact angle fluctuated slightly. From **Figure 10D**, the corrosion products increased significantly when immersion time was up to 6°days, and the corresponding water contact angles fluctuated sharply, but the CA values maintained at around 140. On the basis of the above result, it can be concluded that the super-hydrophobic LDH films presented excellent stability in the high concentration corrosion fluid due to the stable micro/nanostructures on metal surface.

4 CONCLUSION

In this work, super-hydrophobic LDH films have been fabricated successfully by a facile method. The conclusions were obtained as follows:

1 The super-hydrophobic LDHs can be prepared on the surface of etched AZ31 substrate *via in situ* growth hydrothermal crystallization, followed by the modification of PFOTMS. The structure of LDH film was composed of small islands and LDH crystal nanosheets, which provided micro/nanoscale roughness structure to manufacture super-hydrophobic surface.
2 The contact angle was influenced evidently by the surface roughness. The surface roughness of LDH films increased gradually with increasing hydrothermal time or temperature. The highest water contact angle of the film was up to about 163.
3 The super-hydrophobic LDH films can effectively improve the corrosion resistance of the AZ31 Mg alloy. The corrosion current density of samples with the best corrosion resistance was approximately four orders of magnitude lower than that of AZ31 substrate. The corrosion resistance of super-hydrophobic LDH film increased with the increased hydrothermal time or temperature.
4 The obtained super-hydrophobic LDH film still can keep above 140° after immersed in 3.5 wt% NaCl solution for 6 days, indicating the good stability of the super-hydrophobic LDH film.

DATA AVAILABILITY STATEMENT

The original contributions presented in the study are included in the article/**Supplementary Material**. Further inquiries can be directed to the corresponding authors.

AUTHOR CONTRIBUTIONS

XH and JH were responsible for the experimental ideas, methodology and paper writing. YW carried out the acquisition of supplementary data. TX and WX guided the trial process and the paper revision. LW and YC participated in part of data analysis work.

FUNDING

This work was supported by the Natural Science Foundation of Chongqing (cstc2018jcyjAX0450, cstc2019jcyj-msxmX0566), Scientific and Technological Research Program of Chongqing Municipal Education Commission (KJKJQN201800102, KJQN201800619), Visiting Scholar Foundation of Key Laboratory of Biorheological Science and Technology (Chongqing University), Ministry of Education of China (No.CQKLBST-2015-003), Chongqing Special Key Project of Technology Innovation and Application Development, China (Grant No. cstc2019jscx-dxwtBX0016), and the grant project of "Preparing process and properties of antibacterial ureteric stent material with degradable and portable" (H20200113).

ACKNOWLEDGMENTS

We thank Analytical and Testing Center of Chongqing University for performing SEM test and National Engineering Research Center for Magnesium Alloys for XRD, FT-IR, and electrochemical experiments.

SUPPLEMENTARY MATERIAL

The Supplementary Material for this article can be found online at: https://www.frontiersin.org/articles/10.3389/fmats.2021.743112/full#supplementary-material

REFERENCES

Bocchetta, P., Chen, L.-Y., Tardelli, J. D. C., Reis, A. C. d., Almeraya-Calderón, F., and Leo, P. (2021). Passive Layers and Corrosion Resistance of Biomedical Ti-6Al-4V and β-Ti Alloys. *Coatings* 11 (5), 487. doi:10.3390/COATINGS11050487

Cao, Y., Zheng, D., Li, X., Lin, J., Wang, C., Dong, S., et al. (2018). Enhanced Corrosion Resistance of Superhydrophobic Layered Double Hydroxide Films with Long-Term Stability on Al Substrate. *ACS Appl. Mater. Inter.* 10 (17), 15150–15162. doi:10.1021/acsami.8b02280

Chen, H., Zhang, F., Fu, S., and Duan, X. (2006). *In Situ* microstructure Control of Oriented Layered Double Hydroxide Monolayer Films with Curved Hexagonal Crystals as Superhydrophobic Materials. *Adv. Mater.* 18 (23), 3089–3093. doi:10.1002/adma.200600615

Chen, J.-l., Fang, L., Wu, F., Zeng, X.-g., Hu, J., Zhang, S.-f., et al. (2020). Comparison of Corrosion Resistance of MgAl-LDH and ZnAl-LDH Films Intercalated with Organic Anions ASP on AZ31 Mg Alloys. *Trans. Nonferrous Met. Soc. China* 30 (9), 2424–2434. doi:10.1016/s1003-6326(20)65389-4

Chen, J., Song, Y., Shan, D., and Han, E.-H. (2013). Modifications of the Hydrotalcite Film on AZ31 Mg alloy by Phytic Acid: The Effects on Morphology, Composition and Corrosion Resistance. *Corrosion Sci.* 74, 130–138. doi:10.1016/j.corsci.2013.04.034

Chen, J., Wu, L., Ding, X., Liu, Q., Dai, X., Song, J., et al. (2021a). Effects of Deformation Processes on Morphology, Microstructure and Corrosion Resistance of LDHs Films on Magnesium alloy AZ31. *J. Mater. Sci. Tech.* 64, 10–20. doi:10.1016/j.jmst.2019.10.007

Chen, L.-Y., Zhang, H.-Y., Zheng, C., Yang, H.-Y., Qin, P., Zhao, C., et al. (2021b). Corrosion Behavior and Characteristics of Passive Films of Laser Powder Bed Fusion Produced Ti-6Al-4V in Dynamic Hank's Solution. *Mater. Des.* 208, 109907. doi:10.1016/j.matdes.2021.109907

Pazokifard, S., Mirabedini, S. M., Esfandeh, M., and Farrokhpay, S. (2012). Fluoroalkylsilane Treatment of TiO2 Nanoparticles in Difference pH Values: Characterization and Mechanism. *Adv. Powder Tech.* 23 (4), 428–436. doi:10.1016/j.apt.2012.02.006

Qin, P., Chen, L. Y., Zhao, C. H., Liu, Y. J., Cao, C. D., Sun, H., et al. (2021). Corrosion Behavior and Mechanism of Selective Laser Melted Ti35Nb alloy Produced Using Pre-alloyed and Mixed Powder in Hank's Solution. *Corrosion Sci.* 189, 109609. doi:10.1016/j.corsci.2021.109609

Song, Y., Tang, Y., Fang, L., Wu, F., Zeng, X., Hu, J., et al. (2021). Enhancement of Corrosion Resistance of AZ31 Mg Alloys by One-step *In Situ* Synthesis of ZnAl-LDH Films Intercalated with Organic Anions (ASP, La). *J. Magnesium Alloys* 9 (2), 658–667. doi:10.1016/j.jma.2020.03.013

Tang, Y., Wu, F., Fang, L., Guan, T., Hu, J., and Zhang, S. (2019). A Comparative Study and Optimization of Corrosion Resistance of ZnAl Layered Double Hydroxides Films Intercalated with Different Anions on AZ31 Mg Alloys. *Surf. Coat. Tech.* 358, 594–603. doi:10.1016/j.surfcoat.2018.11.070

Wang, P., Zhang, D., Qiu, R., and Hou, B. (2011). Super-hydrophobic Film Prepared on Zinc as Corrosion Barrier. *Corrosion Sci.* 53 (6), 2080–2086. doi:10.1016/j.corsci.2011.02.025

Wang, X., Jing, C., Chen, Y., Wang, X., Zhao, G., Zhang, X., et al. (2020). Active Corrosion protection of Super-hydrophobic Corrosion Inhibitor Intercalated Mg-Al Layered Double Hydroxide Coating on AZ31 Magnesium alloy. *J. Magnesium Alloys* 8 (1), 291–300. doi:10.1016/j.jma.2019.11.011

Wu, L., Ding, X., Zheng, Z., Tang, A., Zhang, G., Atrens, A., et al. (2021). Doublely-doped Mg-Al-Ce-V2o74- LDH Composite Film on Magnesium alloy AZ31 for Anticorrosion. *J. Mater. Sci. Tech.* 64, 66–72. doi:10.1016/j.jmst.2019.09.031

Wu, L., Wu, J., Zhang, Z., Zhang, C., Zhang, Y., Tang, A., et al. (2019). Corrosion Resistance of Fatty Acid and Fluoroalkylsilane-Modified Hydrophobic Mg-Al LDH Films on Anodized Magnesium alloy. *Appl. Surf. Sci.* 487, 569–580. doi:10.1016/j.apsusc.2019.05.121

Xie, J., Hu, J., Lin, X., Fang, L., Wu, F., Liao, X., et al. (2018). Robust and Anti-corrosive PDMS/SiO2 Superhydrophobic Coatings Fabricated on Magnesium Alloys with Different-Sized SiO2 Nanoparticles. *Appl. Surf. Sci.* 457, 870–880. doi:10.1016/j.apsusc.2018.06.250

Xu, C., Chen, L.-Y., Zheng, C.-B., Zhang, H.-Y., Zhao, C.-H., Wang, Z.-X., et al. (2021). Improved Wear and Corrosion Resistance of Microarc Oxidation Coatings on Ti-6Al-4V alloy with Ultrasonic Assistance for Potential Biomedical Applications. *Adv. Eng. Mater.* 23 (4), 2001433. doi:10.1002/adem.202001433

Yang, H., Wu, L., Jiang, B., Liu, W., Song, J., Huang, G., et al. (2021). Clarifying the Roles of Grain Boundary and Grain Orientation on the Corrosion and Discharge Processes of α-Mg Based Mg-Li Alloys for Primary Mg-Air Batteries. *J. Mater. Sci. Tech.* 62, 128–138. doi:10.1016/j.jmst.2020.05.067

Yao, W., Liang, W., Huang, G., Jiang, B., Atrens, A., and Pan, F. (2020). Superhydrophobic Coatings for Corrosion protection of Magnesium Alloys. *J. Mater. Sci. Tech.* 52, 100–118. doi:10.1016/j.jmst.2020.02.055

Zhang, G., Wu, L., Tang, A., Ma, Y., Song, G.-L., Zheng, D., et al. (2018). Active Corrosion protection by a Smart Coating Based on a MgAl-Layered Double Hydroxide on a Cerium-Modified Plasma Electrolytic Oxidation Coating on Mg alloy AZ31. *Corrosion Sci.* 139, 370–382. doi:10.1016/j.corsci.2018.05.010

Zhang, L.-C., Chen, L.-Y., and Wang, L. (2020). Surface Modification of Titanium and Titanium Alloys: Technologies, Developments, and Future Interests. *Adv. Eng. Mater.* 22 (5), 1901258. doi:10.1002/adem.201901258

Zhang, X., Wu, G., Peng, X., Li, L., Feng, H., Gao, B., et al. (2015). Mitigation of Corrosion on Magnesium alloy by Predesigned Surface Corrosion. *Sci. Rep.* 5, 17399. doi:10.1038/srep17399

Zhou, M., Pang, X., Wei, L., and Gao, K. (2015). Insitu Grown Superhydrophobic Zn-Al Layered Double Hydroxides Films on Magnesium alloy to Improve Corrosion Properties. *Appl. Surf. Sci.* 337, 172–177. doi:10.1016/j.apsusc.2015.02.086

Conflict of Interest: The authors declare that the research was conducted in the absence of any commercial or financial relationships that could be construed as a potential conflict of interest.

Publisher's Note: All claims expressed in this article are solely those of the authors and do not necessarily represent those of their affiliated organizations, or those of the publisher, the editors and the reviewers. Any product that may be evaluated in this article, or claim that may be made by its manufacturer, is not guaranteed or endorsed by the publisher.